Ultrasonic Characterization of Microstructures in Inertia Friction Welds on SiC-Reinforced 8009 Aluminum

Ultrasonic techniques allowed rapid determination of the patterns of flow lines in the welds as well as the dimensions of the various weld zones as functions of position

BY T. J. LIENERT, P. B. NAGY AND W. A. BAESLACK III

ABSTRACT. The microstructures of inertia-friction welds (IFRWs) on an aluminum metal matrix composite have been investigated using several ultrasonic examination (UE) techniques as well as standard characterization methods. This study represents one of the first efforts to utilize UE methods for microstructural characterization of welds. The flow line patterns and dimensions of the different weld zones in IFR welds on a SiC-reinforced 8009 aluminum composite (8009/SiC/11p) have been determined using optical microscopy (OM) and scanning-electron microscopy (SEM) as well as the following UE methods: 1) acoustic microscopy, 2) C-scan imaging, 3) axial backscattering, and 4) radial backscattering. The UE techniques exploited the variations in ultrasonic scattering produced by changes in the distribution of the SiC particles.

The ultrasonic procedures allowed rapid determination of microstructural features in the IFR welds. The acoustic microscopy technique provided detailed pictures of the flow lines in longitudinal sections of the welds, as well as the dimensions of the different weld zones as functions of radial position. Ultrasonic C-scan imaging determined the flow line patterns in thin disks centered at different axial distances from the weld centerline. The C-scan imaging technique also revealed the presence of purposely induced defects that resulted from lack of bonding near the axial centerline of one of the welds. Axial ultrasonic backscattering measurements were used to determine the widths of the various weld zones as functions of radial position. Finally, radial ultrasonic backscattering measurements provided the overall widths of the entire weld zone at a fixed radial position.

The results of this study were self-consistent in that weld microstructures and dimensions determined with one UE technique correlated closely with those found with other UE techniques, as well as with OM and SEM. The ultrasonic methods complement OM and SEM by providing similar microstructural information over the size scales examined. The UE techniques described in this study may also be employed to study IFR welds on similar materials and can likely be adapted to other processes involving metal matrix composites (MMCs) and comparable materials.

The information determined from this study also contributes to an improved understanding of process/structure/property relations for IFR welds on 8009/SiC/11p as well as plastic flow resulting from the IFRW process. The SiC particles in the as-received extrusion were distributed into alternate SiC-rich and SiC-depleted bands oriented parallel to the extrusion direction. The flow lines of SiC-rich and SiC-depleted bands followed spiral-shaped paths in the IFR welds. Lower values for strain to failure and elastic modulus (relative to the base material) in subscale tensile samples from these welds tested in previous studies are attributed to the realignment of the bands during IFRW. Results confirm that flow in the IFR welds took place with components in the axial, radial and tangential directions. Moreover, the strength or dominance of the components of flow varied with axial and radial position for a constant weld axial force. The strength of the various flow components also changed with the axial force used for welding. The information on the final patterns of flow lines and weld dimensions may be useful in corroborating the final results of computational process models for IFRW.

KEY WORDS

Ultrasonic Examination
SiC Reinforced
MMC
Composites
Aluminum
Friction Weld
Microstructure
Inertia-Friction

T. J. LIENERT is with the Department of Materials Science and Engineering and W. A. BAESLACK III is with the College of Engineering, The Ohio State University, Columbus, Ohio. P. B. NAGY is with the Department of Aerospace Engineering and Engineering Mechanics, University of Cincinnati, Cincinnati, Ohio.

Paper presented at the 77th Annual AWS Meeting, held April 21–25, 1996, Chicago, Ill.

Introduction

Advances in materials science over the last few decades have driven the commercial development of several classes of novel materials with microstructures and properties that are tailored to specific applications. Aluminum metal matrix composites (Al MMCs) represent one of the many classes of engineered materials. Al MMCs combine the ductility and toughness of an Al alloy matrix with the stiffness of a low-density ceramic reinforcement. Due to their high specific strength and modulus relative to monolithic Al products, Al-MMCs are candidates for structural applications in the aerospace and automotive industries.

Both wrought and cast precipitation-hardenable aluminum alloys are used as the matrix, as well as the newer rapidly solidified/powder metallurgy (RS/PM) alloys. Typical reinforcement materials include boron (B), graphite (C), silicon carbide (SiC), and aluminum oxide (Al_2O_3), and the reinforcement may take the form of whiskers, particles, or chopped or continuous fibers. While much of the early research on Al-MMCs concentrated on continuous fiber materials, recent investigations have focused on discontinuously *(i.e.,* particle, whisker or chopped fiber) reinforced aluminum (DRA) alloy MMCs. The growing interest in DRAs is primarily due to their lower cost of production and their relatively isotropic properties.

High-temperature DRAs (HTDRAs) have been commercially produced by blending crushed ribbons of RS AA 8009 with 3 μm SiC particulate followed by hot pressing and extruding to size (Ref. 1). The 8009 aluminum alloy matrix (Al-8.5 Fe-1.7 Si-1.3 V, wt-%) is strengthened by a uniform distribution of fine intermetallic dispersoids that form during the RS process and subsequent consolidation and thermomechanical processing (TMP) operations (Refs. 2–4). These dispersoids are stable to temperatures approaching 375°C and have very low coarsening rates at working temperatures. The fine dispersoids, as well as a small α-aluminum grain size resulting from RS processing, give the 8009 alloy superior high-temperature mechanical properties relative to conventional Al alloys (Ref. 5). The addition of 11 vol-% SiC particles (SiC_p) to the 8009 matrix alloy results in an MMC (8009/SiC/11p) with increased specific strength and stiffness at elevated temperatures (Refs. 6, 7). Potential applications for 8009/SiC/11p include aircraft wing skins, missile bodies and other aerospace structures that are heated aerodynamically or that reside in close proximity to the engines.

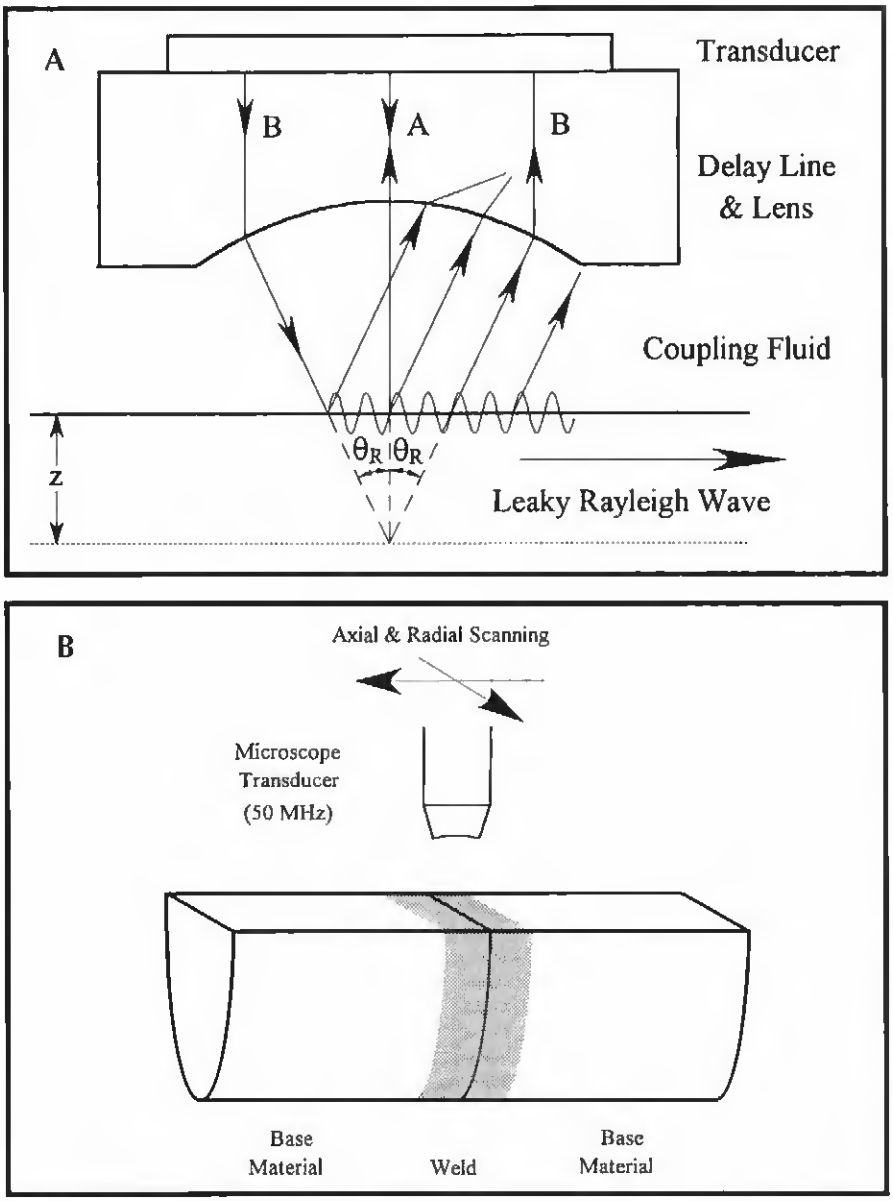

Fig. 1 — A — Geometrical configuration of reflection type acoustic microscope; B — sample and scanning geometry for acoustic microscopy.

Effective use of the 8009/SiC/11p MMC will often depend upon its ability to be joined both to itself and to dissimilar materials. Since the properties of this composite derive from its unique microstructure, welding processes must be chosen that limit grain and dispersoid coarsening, as well as avoid chemical reactions between the SiC particles and the matrix. Solid-state welding processes, such as inertia friction welding (IFRW), appear to offer greater control over microstructures during welding of RS Al alloys (Ref. 8) and Al-MMCs (Ref. 9) than fusion welding processes.

Friction welding (FRW) produces welds between parts held in compression that move relative to one another. The process is largely solid-state in nature. The heat of welding originates from direct conversion of the mechanical energy of the moving part(s) to thermal energy and strain energy (Refs. 10, 11). More than 90% of the energy consumed in plastic deformation is transformed into heat, although a small fraction of the energy is stored in the material as strain energy (Ref. 12). Application of an axial compressive force maintains intimate contact of the parts and promotes plastic deformation of the material at the faying surfaces during welding.

There are two major process variations for FRW: direct-drive welding and inertia welding (Ref. 13). The distinction between the two variations lies in the method of energy delivery to the weld. In direct-drive FRW, the moving part is con-

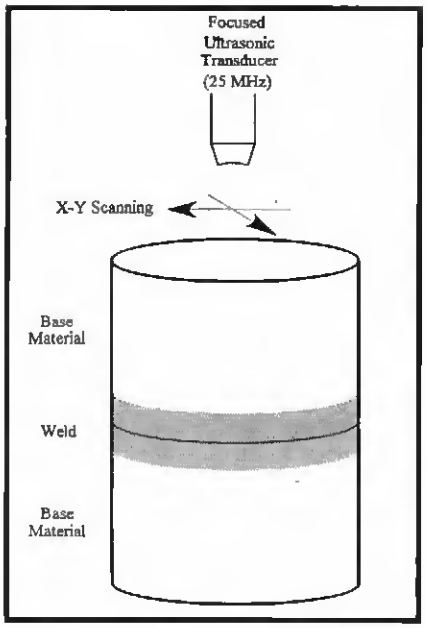

Fig. 2 — Sample and scanning geometry for ultrasonic C-scan imaging.

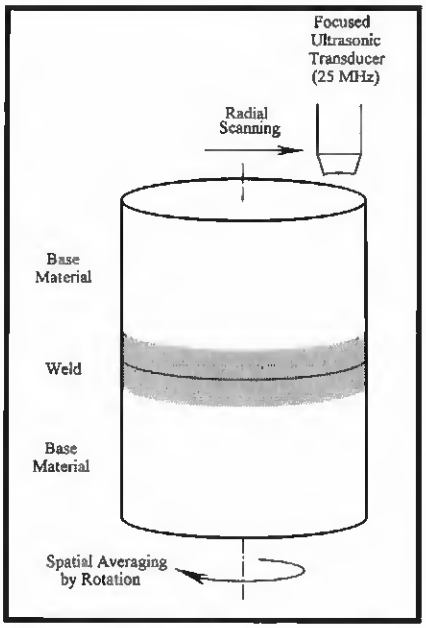

Fig. 3 — Sample and scanning geometry for axial backscattering measurements.

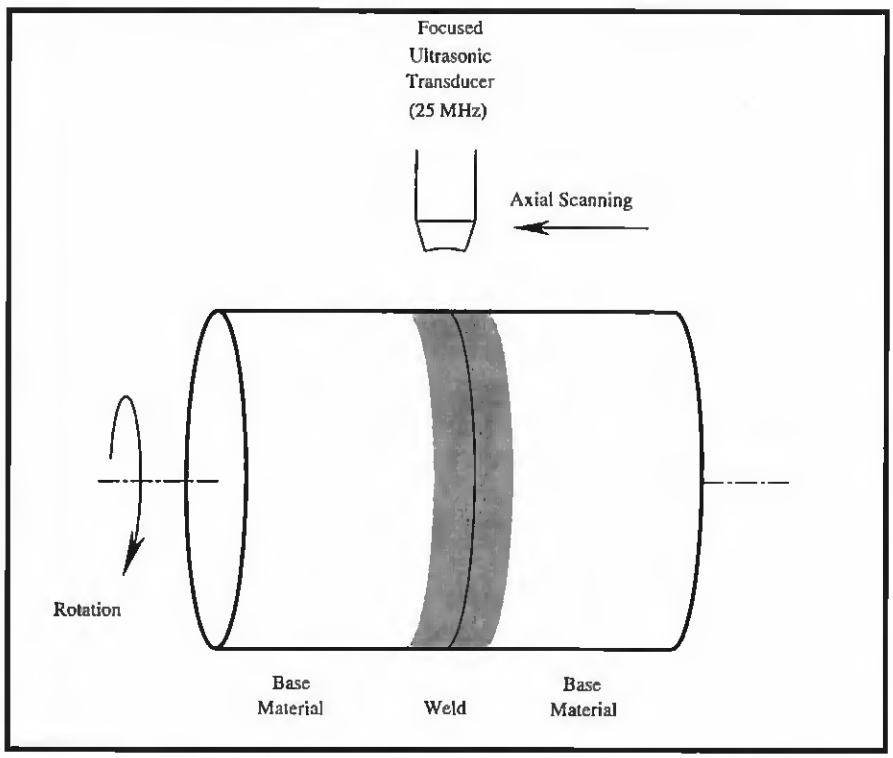

Fig. 4 — Sample and scanning geometry for backscattering measurements from the radial direction.

tinuously driven by a motor at a constant speed. A brake is applied to terminate the process after a preset time, and the axial pressure is then typically increased to aid in consolidation of the joint. Inertia FRW (IFRW) employs the stored energy of a decelerating flywheel attached to the rotating part to effect the weld. IFRW is normally performed with a constant axial force. The thermal cycle for most IFR welds is typically much shorter (~ 1 to 2 seconds) than that for direct-drive welds (~ 10 to 20 seconds) (Ref. 14).

The rapid thermal cycle and solid-state nature of IFRW are well suited for the joining of advanced materials. IFRW has been employed to successfully join several high-temperature Al-Fe alloys strengthened by intermetallic dispersoids (Refs. 15–18), as well as MMCs with conventional Al alloy matrices (Refs. 19–23) and oxide dispersion strengthened (ODS) materials (Refs. 24, 25). However, a greater understanding of process/microstructure/property relations is needed for successful IFR welding of Al-MMCs with minimal loss of properties.

The microstructural changes that take place during IFRW are similar to those that occur during hot working and forging. In fact, IFRW is often classified as a forge welding process. Displacement of material during working results in the development of microstructural features, referred to as flow lines, that are aligned with the working direction. The fracture resistance of forged products is known to improve when the flow lines are oriented parallel to major stress trajectories and perpendicular to potential crack paths (Ref. 26). Knowledge of the patterns of the plastic flow lines in IFR welds is important in view of this relationship between weld microstructures and resulting properties.

Microstructural characterization of welds typically employs optical microscopy (OM) and scanning electron microscopy (SEM) as well as X-ray diffraction (XRD) and transmission electron microscopy (TEM) on occasion. While most previous ultrasonic examination (UE) of welds has concentrated on flaw detection (Refs. 27, 28), UE of various weld zones has been recently shown to yield useful information on similar and dissimilar metal IFR welds in aluminum, steel and copper (Refs. 29, 30). UE methods have also been successfully employed to examine microstructural features of IFR welds in 8009/SiC/11p (Ref. 31).

Ultrasonic examination employs piezoelectric transducers that deliver high-frequency (ultrasonic) elastic waves into the material being inspected and sense their return (Refs. 27, 28). These elastic waves induce mechanical vibrations in the material as they propagate. A couplant such as water, alcohol, glycerin, or oil is normally used to enhance transmission of the ultrasonic waves between the transducer and test material. Ultrasonic examination is very sensitive to local changes in elastic modulus (stiffness) and density, and can be used to detect gross changes in these properties caused by the presence of defects or a second phase.

The two major objectives of this study are 1) to demonstrate the utility of UE techniques as tools for microstructural characterization of IFR welds in

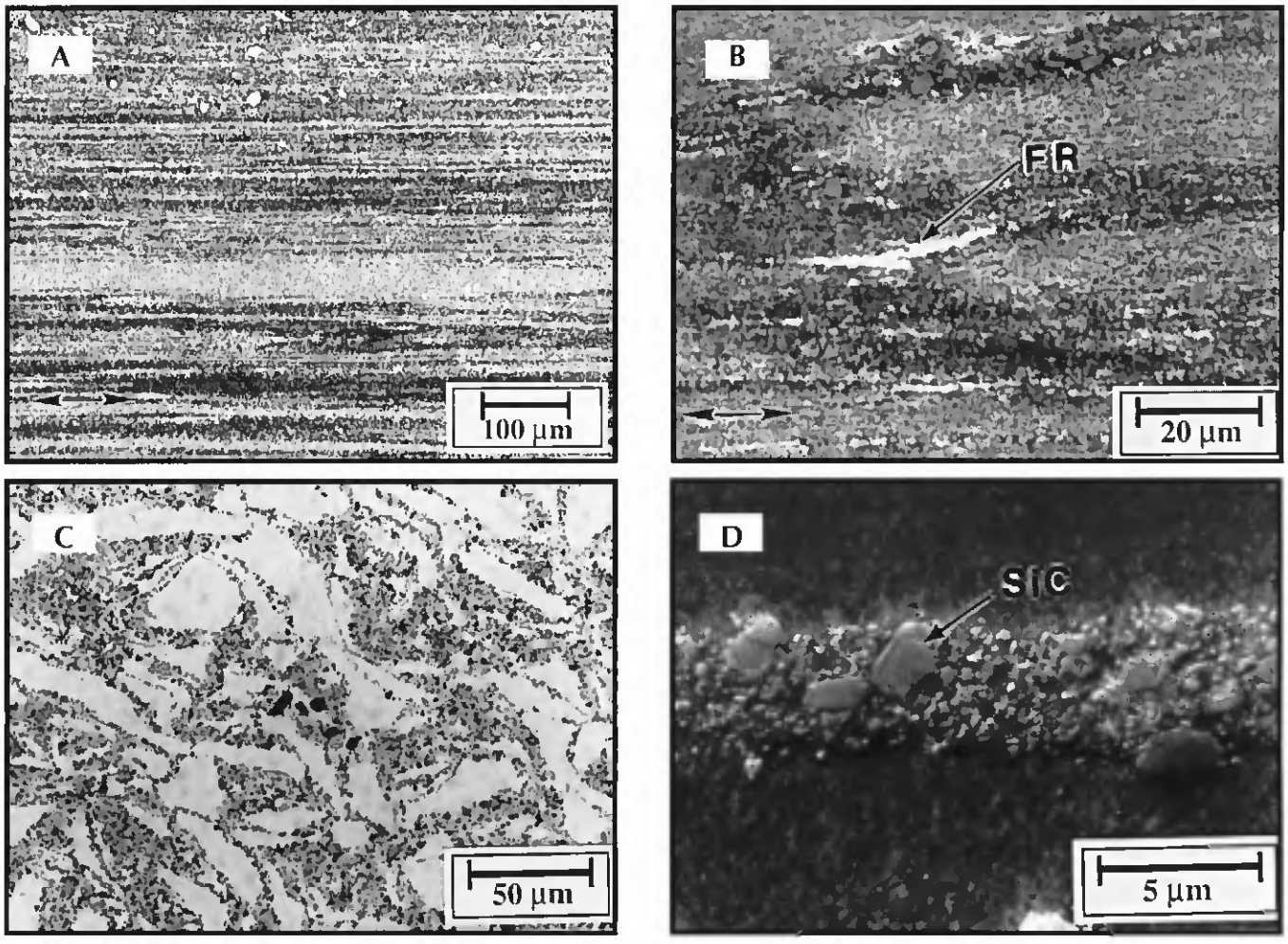

Fig. 5 — Micrographs of 8009/SiC/11p extruded base material: A, B — optical micrographs from longitudinal section; C — optical micrograph from transverse section; D — SEM micrograph in SE mode. Horizontal arrows in A and B indicate extrusion direction. Several very large SiC particles are visible in A. FR in B indicates featureless region. Arrow in D indicates SiC particle.

8009/SiC/11p and 2) to determine the patterns of plastic flow lines and the dimensions of the different weld zones in the same IFR welds. The microstructures of the IFR welds are examined with OM, SEM and several UE methods. The advantages and applications of the UE techniques are discussed, as well as the process implications of this study and process/structure/property relations for IFR welding of 8009/SiC/11p.

Experimental Procedure

A 3.6-in. (9-cm) diameter experimental extrusion of 8009/SiC/11p material was supplied by AlliedSignal, Inc. (Morristown, N.J.). Cylindrical samples, 1 in. (2.5 cm) in diameter and 2.5 in. (6.3 cm) in length, were machined from the extrusion with the 2.5-in. dimension parallel to the extrusion direction. Joining was performed with an MTI model 120B inertia welding system.

The welding parameters were identical to those used in previous work on monolithic Al-Fe-Si-V alloys (Refs. 17, 18) except that higher axial forces were used for the 8009/SiC/11p MMC. The samples were IFR welded at 5000 rpm (524 rad/s) using a moment of inertia (wk^2) of 3.93 lb ft^2 (0.17 kg m^2). These parameters gave an initial flywheel energy of 16.7 x 10^3 ft lb (22.9 kJ). Welds were produced at two different levels of axial force: 24.8 x 10^3 lb (111.6 kN) and 34.7 x 10^3 lb (156.2 kN). The welds are hereafter referred to as the low axial force (LAF) welds and the high axial force (HAF) welds, respectively. Welding time for both levels of axial force was less than two seconds.

The microstructures of the welded samples were initially characterized using optical microscopy (OM) and scanning electron microscopy (SEM). Metallographic specimens were prepared from each weld using standard practice. Final polishing was performed using a colloidal silica suspension. Specimens for optical microscopy were not etched. Selected specimens were also carbon-coated and examined using SEM.

Separate HAF and LAF weld specimens were also studied using four ultrasonic techniques: 1) acoustic microscopy, 2) C-scan imaging, 3) axial backscattering and 4) radial backscattering. Details of each of the ultrasonic techniques are presented in the following paragraphs. Further information on the techniques can be found in Refs. 27–32. Two sets of samples were prepared for UE. One set was used for acoustic microscopy, while the second set was used for C-scan imaging and the two backscattering techniques. The samples examined with acoustic microscopy were prepared and welded exactly as described above.

The radial backscattering technique required removal of the weld flash but was completely nondestructive since no sectioning or machining of the weld region was performed. C-scan imaging and axial backscattering measurements were performed on the same samples used for radial backscattering, although removal of the weld flash was not required for

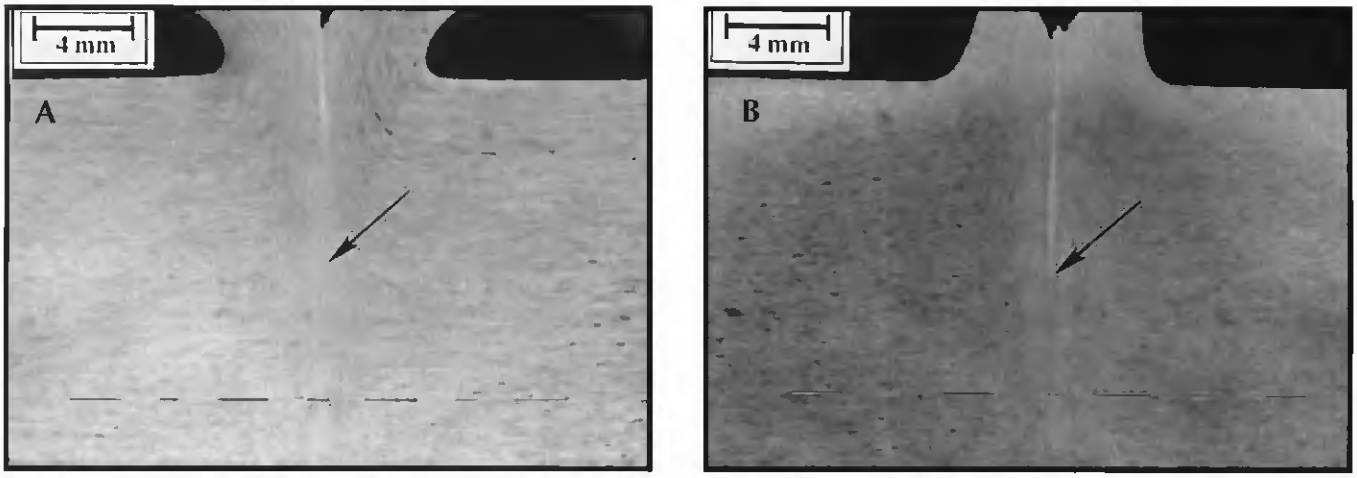

Fig. 6 — Optical macrograph. A — HAF weld; B — LAF weld. The dashed lines denote the location of the axial centerline. Arrows indicate the weld centerline.

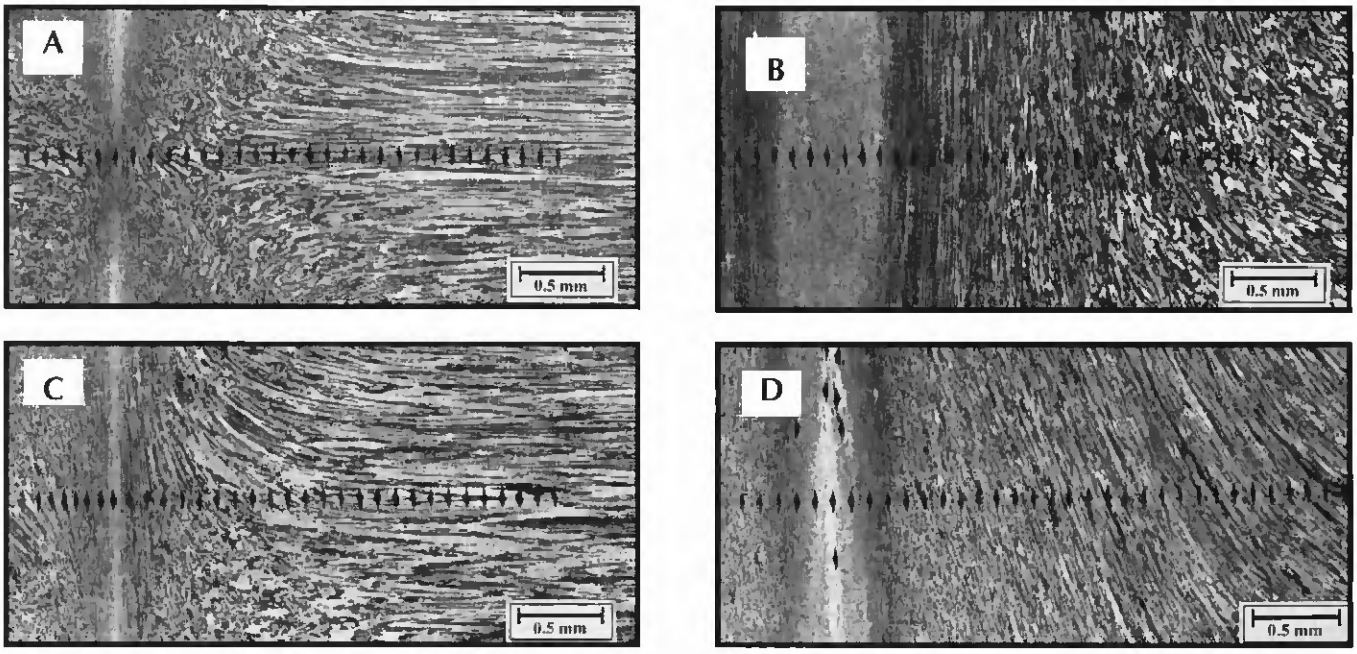

Fig. 7 — Optical micrographs from longitudinal sections. A — A HAF weld near the axial centerline; B — HAF weld near the widest part of the IHDZ; C — A LAF weld near the axial centerline; D — LAF weld near the widest part of the IHDZ.

these two methods. Samples for C-scan imaging and backscattering measurements were prepared and welded exactly as described above with one exception. In an attempt to introduce small defects, a small turning center (60-deg cone angle, ~ 0.03 in. deep) was left on the face of one of the pieces used to produce a LAF weld. Turning centers facilitate easy machining of the cylinders on a lathe and are normally removed before welding with a facing operation.

Of the currently available ultrasonic inspection methods, scanning acoustic microscopy is the closest to optical microscopy in terms of resolution, limited penetration depth and sample preparation. While commercial high-frequency acoustic microscopes can attain lateral resolutions of a few microns, the 50 MHz low-frequency version used in this study offered approximately 200 μm lateral resolution at a penetration depth of 50 μm.

Figure 1A shows the geometrical configuration of a reflection-type scanning acoustic microscope. The acoustic microscopy technique described here was not entirely nondestructive, since the sample was sectioned in half longitudinally for examination, as shown in Figure 1B. Polishing and etching of the section was not required for inspection. The main acoustic contrast with this technique originated from those rays (such as B in Figure 1A) that meet the interface at a special angle called the Rayleigh angle (θ_R) and generate "leaky" Rayleigh waves running along the surface of the sample (Ref. 32). As the Rayleigh waves propagate along the surface, a small amount of the wave energy is lost as it "leaks" back across the interface resulting in attenuation of the surface waves. A special wide-angle (60-deg angle of convergence) spherical ultrasonic transducer was focused slightly below the surface to measure the reflection coefficient (R) as a function of position as the transducer was scanned axially and radially across the sectioned sample — Fig. 1B. Broadband surface wave detection was used in this

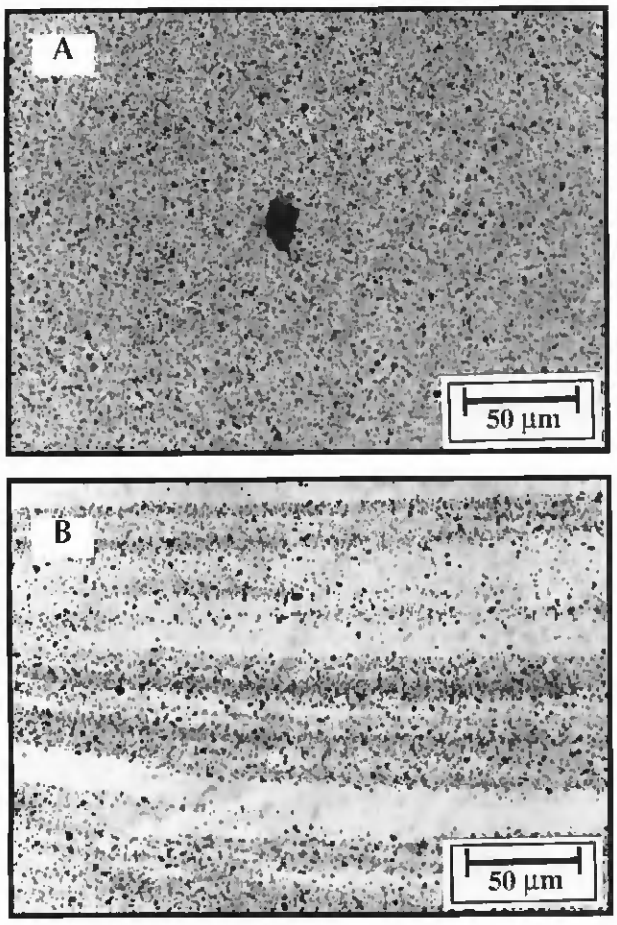

Fig. 8 — Optical micrographs from a transverse section of a LAF weld. A — IHDZ; B — OHDZ. A very large SiC particle is visible in the center of A.

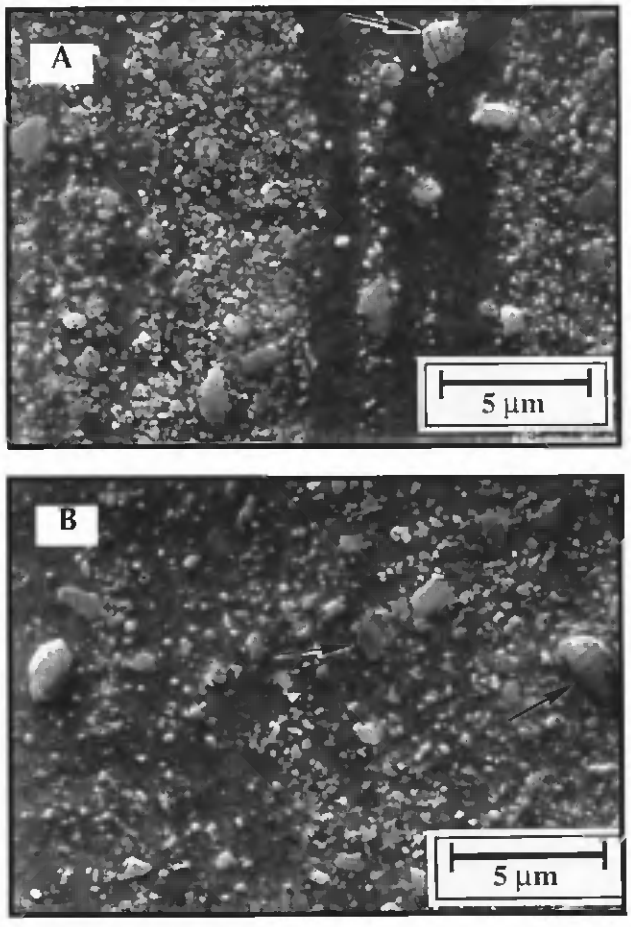

Fig. 9 — SEM micrographs of a HAF weld. A — OHDZ; B — IHDZ. Arrows indicate cracked SiC particles.

experiment to optimize contrast. Ethyl alcohol was employed as a couplant. The micrographs were formed by directly mapping the amplitude of the surface waves, which was strongly attenuated by inhomogeneities in the near-surface region of the specimen.

Figure 2 shows the experimental configuration used for ultrasonic C-scan imaging. A 25-MHz, 25-mm (1-in.) focal length immersion transducer was used to map the ultrasonic backscattering intensity from different depths as the transducer was rastered across the end of the sample. This transducer provided a lateral resolution of approximately 500 µm. At each location, the total backscattered signal was first gated to separate components originating from the desired depth from those of the rest of the signal. The depth of the selected layer was varied by changing the delay of the gating signal. A gating time of 0.1 µs was used, corresponding to a layer approximately 0.36 mm (0.014 in.) thick. The ultrasonic image was constructed from the amplitude of the ultrasonic signal within the gate, which was a function of the extent of local inhomogeneity of the material in the layer.

Figure 3 shows the configuration used for axial ultrasonic backscattering measurements. The transducer and frequency used for this technique were the same as used for C-scan imaging. With this technique, the transducer was scanned radially across the end of the sample. The backscattered ultrasonic signal was essentially a random function of time with zero mean (dc component) and higher variance (ac component) at times corresponding to the depth of more inhomogeneous layers. At each radial position, the backscattered signal was first squared to obtain the ultrasonic intensity as a function of depth. The backscattered intensity was then averaged for points of identical radial distance from the axis by rotating the specimen.

Figure 4 is a schematic diagram for the ultrasonic backscattering measurements from the radial direction. A 25-MHz, 25-mm focal length immersion transducer was used to measure the ultrasonic backscattering from a 3-mm (0.12-in.) wide region at a depth of 4 mm (0.16 in.) below the surface. The transducer was scanned parallel to the axis over a length of approximately 70 mm (2.8 in.) as the specimen was slowly rotated. Rotating the specimen allowed averaging of the backscattered intensity for points at the same radial distance from the axial centerline.

Results

Optical and Electron Microscopy

Base Material

Optical micrographs of the 8009/SiC/11p base material are shown in Fig. 5A–C. Figures 5A and B were taken on a longitudinal section (*i.e.*, parallel to the extrusion direction) of the base material, while Fig. 5C was taken on a transverse section. Figure 5A depicts a cluster of fairly large (~15 µm) SiC particles distributed in the RS matrix. Pieces of the crushed RS ribbon of 8009 were elongated during extrusion resulting in a banded or striated microstructure. Individual bands of the base material extending several hundred microns in length were also discernible in Fig. 5A. Small featureless regions were occasionally observed in the base material — Fig. 5B. The bands displayed an irregular cross section and measured 30 to 50 µm

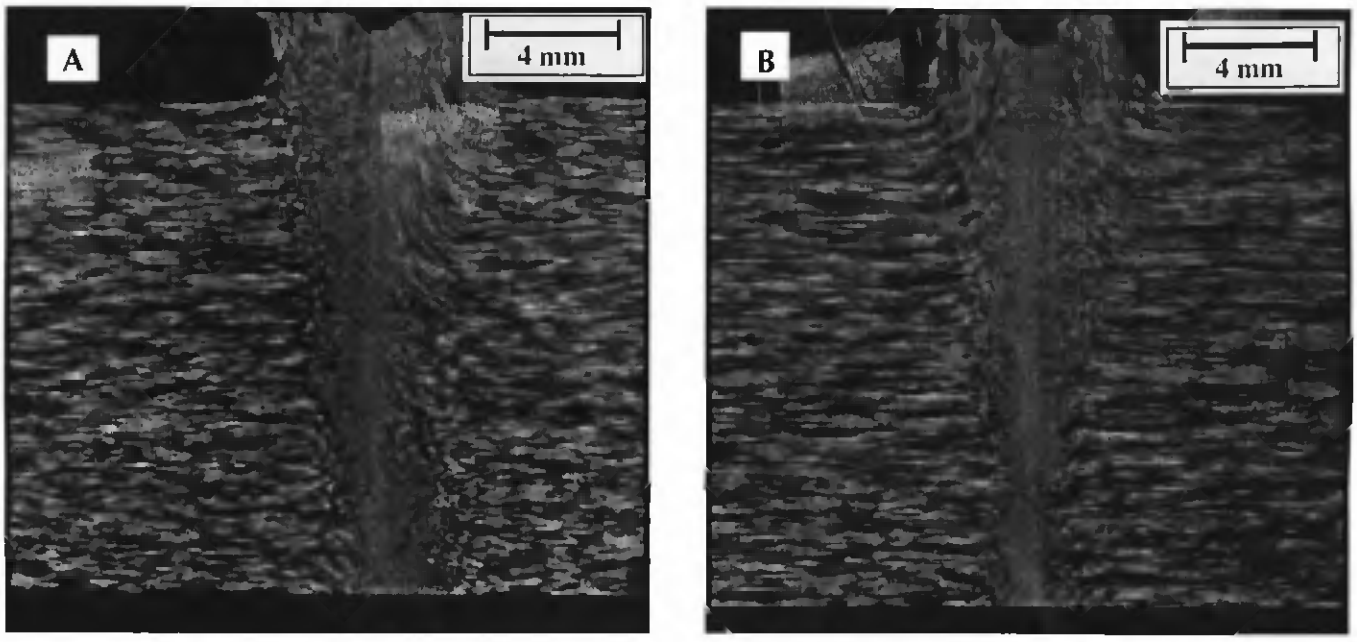

Fig. 10 — Acoustic micrographs. A — HAF weld; B — LAF weld.

across on average, as shown in Fig. 5C.

Examination of the base material at higher magnifications using the SEM revealed that most of the SiC particles were clustered in bands running parallel to the extrusion direction — Fig. 5D. Some areas contained a high volume fraction of SiC, while adjacent areas were nearly devoid of SiC. The nonuniform distribution of SiC was probably due to insufficient kinetic blending during primary production. The majority of the SiC particles were approximately 0.5 to 3 μm in size, although particles as large as 20 μm were observed. Some of the larger SiC particles appeared to be cracked.

Weld Zone

Optical macrographs from longitudinal sections of typical HAF and LAF weld samples are shown in Fig. 6. Note that a longitudinal weld section in this case is defined as that perpendicular to the original faying surfaces. The dashed lines in Fig. 6A and 8 indicate the approximate location of the axial centerline (*i.e.*, the rotation axis during welding) of each weld. Additionally, the arrows indicate the weld centerline. No defects were observed in any of these welds. A symmetrically uniform flash or upset collar was formed around the circumference of each sample during welding. The extent of the upset for the HAF welds was larger than for the LAF welds. The total axial displacement of welding averaged 0.16 in. (0.4 cm) for the LAF welds and 0.35 in. (0.9 cm) for the HAF welds.

Inspection of the longitudinal sections of the welds with OM using higher magnifications revealed the presence of two distinct regions of the weld heat-and-deformation-affected zone (HDZ) — Fig. 7. An inner HDZ (IHDZ) of uniform contrast was visible along the weld centerline. The IHDZ of the welds exhibited a homogeneous microstructure with a relatively uniform distribution of SiC resulting from the extensive intermixing experienced during welding. In these cross sections, the IHDZs appeared narrow near the axial centerline and near the periphery, and wider in between. The outer HDZ (OHDZ) of the welds experienced less deformation and lower peak temperatures, and evidence of realignment of the individual bands was apparent. The OHDZ of the welds widened with increasing radial distance from the axial centerline. The rows of microhardness indentations visible in Fig. 7A and C are coincident with the axial centerline. Results of the microhardness and tensile testing of the IFR welds have been presented elsewhere (Ref. 33).

The IHDZ for the HAF welds varied in width from approximately 0.05 mm (50 μm) at the axial centerline to about 0.65 mm at a position near the 3/4 radius. The overall width of the HDZ was approximately 0.1 mm at the centerline and 8 mm near the periphery. The width of the IHDZs of the LAF welds varied from about 0.05 mm (50 μm) at the axial centerline to approximately 0.25 mm near the 1/2 radius position. The OHDZs of the LAF welds widened from about 0.06mm (60 μm) near the axial centerline to approximately 8 mm near the periphery. The width of the OHDZ for the HAF welds increased more rapidly with radial distance than the OHDZ of the LAF welds.

The optical micrographs in Fig. 8 were taken from transverse sections of a weld sample (transverse sections are defined here as those parallel to the original surfaces). A uniform distribution of SiC is again seen in the IHDZ of the welds — Fig. 8A. A large SiC particle is visible at the center of Fig. 8A. Reorientation or redirection of individual bands in the OHDZ in the radial and tangential directions was also evident — Fig. 8B.

Observations made using optical microscopy were confirmed by SEM. Figure 9A is an SEM micrograph of the OHDZ of a HAF weld, while Fig. 9B is an SEM micrograph of the IHDZ of the same weld. The SiC particles were distributed uniformly throughout the IHDZ, while banding of the reinforcement was observed in the OHDZ. As in the base material, some of the larger SiC particles in the HDZs appeared cracked. Crushing of reinforcement particles during hot deformation of MMCs at high strains has been reported by several researchers (Refs. 34–36) and was not totally unexpected during IFRW. However, it is not clear whether these particles cracked during production of the composite or during IFRW. Nonetheless, no significant differences in the SiC size distribution was noted between the base material and the weld HDZs. Similar observations were made during SEM examination of the LAF welds. Results of additional microstructural characterization of the welds with optical microscopy and SEM have been presented elsewhere (Ref. 33).

Ultrasonic Evaluation

The UE techniques used in this work exploited the variations in ultrasonic scattering provided by the alignment and distribution of SiC particles. The SiC particles in the as-received extrusion were distributed into alternate SiC-rich and SiC-depleted bands oriented parallel to the extrusion direction. The banding of SiC in the base material provided an excellent contrast mechanism for ultrasonic mapping. The higher stiffness of the SiC particles (approximately four times that of the aluminum alloy matrix) together with a slightly higher density assured strong ultrasonic scattering from the SiC-rich bands. Conversely, weaker ultrasonic scattering was associated with the SiC-depleted bands. Determination of the spatial variation of scattering allowed distinction of individual layers. Note that individual SiC particles were not resolved with these techniques.

Plastic flow in the OHDZ during welding resulted in realignment of the bands, while mechanical mixing of the material in the IHDZ produced a uniform distribution of SiC particles. The UE methods allowed distinction between the regions with different microstructural characteristics. The variations in ultrasonic scattering from the three different regions enabled the determination of the sizes of the weld zones and provided information about the flow patterns at different positions in the OHDZ.

Acoustic Microscopy

The acoustic microscopy technique provided detailed images of the flow lines in longitudinal sections of the welds, as well as the widths of the inner and outer HDZs as functions of radial position. The acoustic micrographs for the HAF and LAF welds are shown in Fig. 10. These images clearly show the size and shape of the inner and outer HDZs. The dimensions of the inner and outer HDZs appeared slightly larger in the acoustic micrographs than in the optical micrographs shown previously due partially to the lower resolution of acoustic microscopy. The dark bands in the base material correspond to the SiC-rich layers, while the lighter bands delineate areas that contain little or no SiC. As shown previously in the optical micrographs of Fig. 7, the plastic flow in the OHDZ of this cross section occurred in the radial and axial directions as a result of welding. The characteristic arrangement of flow lines was found to vary with axial force. Specifically, the flow lines were more strongly angled in the radial direction near the periphery of the HAF welds relative to the LAF welds, just as in Fig. 7. The uniform gray contrast of the IHDZ was consistent with the uniform distribution of SiC in this region, as shown in Figs. 7–9.

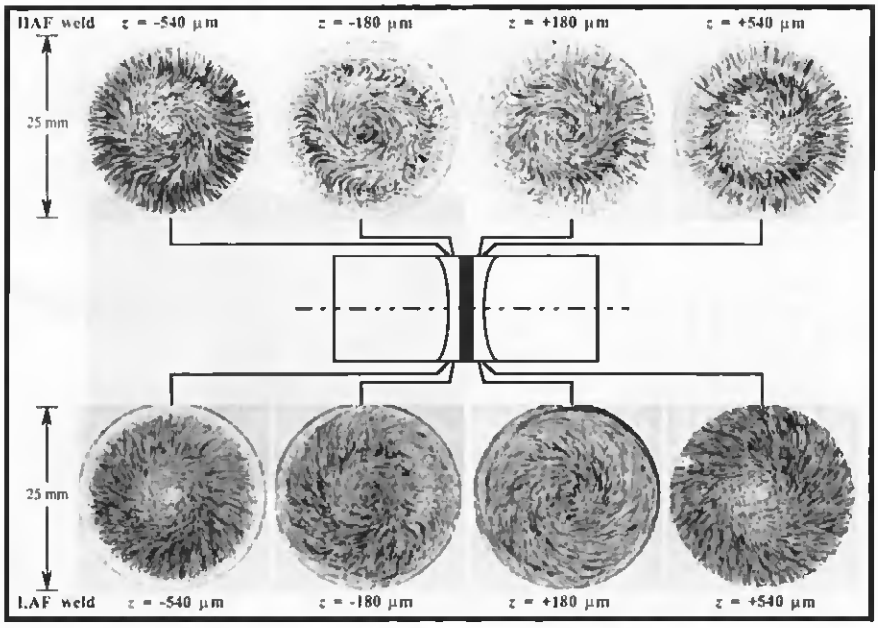

Fig. 11 — C-scan images of HAF weld (upper row) and LAF weld (lower row) at different axial distances above (+) and below (-) the weld centerline.

C-Scan Imaging

Ultrasonic C-scan imaging determined the patterns of flow lines in thin disks oriented parallel to the weld centerline. Figure 11 shows the ultrasonic C-scan images of the flow patterns at different axial distances above (+) and below (-) the weld centerline for the HAF and LAF welds. The positive side of the weld refers to the side where the transducer was placed. The distances shown in Fig. 11 correspond to the distance from the weld centerline to the center plane of a disk 0.36 mm (0.014 in.) thick. Hence, the information depicted in two dimensions in each ultrasonic image was actually collected from a thin disk. The pattern of flow lines in these sections indicated flow with both radial and tangential components. Note that the rotation direction of the flow lines above the weld centerline (+) was opposite to that below the weld centerline (-). Comparison of the flow line patterns at a given distance above and below the weld centerline for a given weld indicates that flow was symmetric about the weld centerline.

Figure 12 provides a comparison of C-scan images of the flow line patterns at the weld centerline and at various positive axial distances from the weld centerline for both welds. The thickness of the homogenized IHDZ layer could not be fully resolved at the frequency used and fragments of the nearby flow lines from both above and below the thin homogenized IHDZ were apparent. At axial distances farther from the weld centerline, flow lines were observed only near the periphery of the weld since the HDZ width was much greater there than near the axial centerline. The C-scan imaging technique also revealed the presence of small defects near the axial centerline of the LAF weld. The ultrasonic C-scan image from the weld centerline of the LAF weld (0 μm position in Fig. 12) exhibits at least three small defects (dark circles indicated by the arrows) near the axial centerline. The defects were also seen in the C-scan images from disks centered at ±180 μm from the weld centerline — Figs. 11, 12. These defects resulted from the presence of the turning center as discussed earlier. Additional examination of the defects using OM showed them to be flat planar defects that apparently resulted from a lack of bonding.

As in Figs. 7 and 10, the flow line patterns were found to vary with axial force. A comparison of the patterns for the two welds obtained at an axial distance of +180 μm is given in Fig. 13A. The spiral-shaped pattern of the LAF weld suggests that plastic flow occurred with large components in both the radial and tangential directions across the entire radial dimension. A similar pattern of flow was observed near the axial centerline of the HAF weld. However, at positions near 2/3 radius of the HAF weld, the tangential component decreased greatly and flow near the periphery of the HAF weld

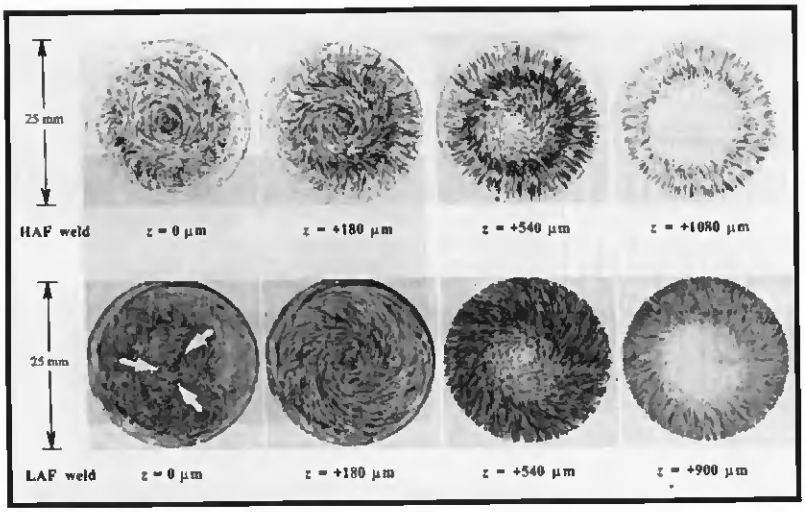

Fig. 12 — C-scan images of HAF weld (upper row) and LAF weld (lower row) at various positive axial distances above the weld centerline. Arrows in section at 0 µm of the LAF weld indicate induced defects.

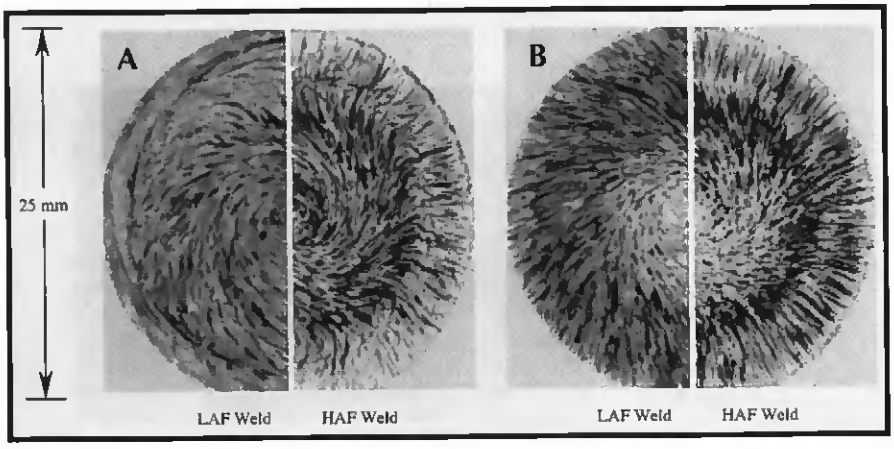

Fig. 13 — C-scan images for LAF and HAF welds at (A) 180 and (B) 540 µm above the weld centerline.

proceeded mainly in the radial direction. Evidence of flow reversal in the form of boomerang-shaped features near the 2/3 radius positions was also observed in the sections of the HAF weld obtained at axial distances of -180 µm — Fig. 11.

A comparison of flow line patterns obtained at axial distances of +540 µm from the weld centerline is shown in Fig. 13B. Again, a spiraled arrangement of flow lines was evident in the LAF weld, but the tangential components at each radial position appeared smaller than those at the respective positions in the section obtained at 180 µm. For the HAF weld, the location of the transition from spiral flow to mainly radial flow in the section obtained at 540 µm was shifted inward to positions near 1/2 radius. No evidence of flow reversal was noted in the HAF weld sections obtained at 540 µm.

Axial Ultrasonic Backscattering

The ultrasonic C-scan imaging technique described above provided detailed maps of the distribution of the flow pattern in different cross sections of the HDZ at various distances from the weld centerline. The corresponding axial distributions at varying radial distances from the axial centerline also contain valuable information on the HDZ structure. The axial distribution can be more easily measured by considering the average backscattered intensity from a small volume rather than resolving individual flow lines within that region.

Axial ultrasonic backscattering measurements were used to determine the widths of the inner and outer HDZs as functions of radial position. Figure 14 shows the averaged axial backscattering profiles from the HAF weld at four different radial distances from the axial centerline. The amplitude of the backscattered signal is given in arbitrary units. Note that direct comparison of the amplitudes between (A), (B), (C) and (D) of Fig. 13 is not possible because different gain settings were used to record the backscattered signals at each different radial position. This result is inconsequential since the most useful information derives from the shapes of the profiles, not from the different relative amplitudes.

The amplitude of the backscattered signal was very sensitive to the orientation of the SiC-rich bands. For example, consider the profile obtained at a radial distance of 1.27 mm (0.051 in.) from the axial centerline — Fig. 14A. At axial distances greater than approximately 0.75 mm (0.03 in.) from the weld centerline, where the bands or striations of the base material were oriented parallel to the incident ultrasonic beam, the amplitude of the backscattered signal was low. At axial distances between 0.75 and 0.25 mm (0.03 and 0.01 in.), the amplitude of the backscattered signal increased with increasing radial components of plastic flow of the bands in the OHDZ. At axial distances less than approximately 0.25 mm (0.01 in.), the amplitude of the backscattered signal fell somewhat due to the homogenous distribution of the SiC particles in the IHDZ. This trend suggests that the average total width of the OHDZ at this radial position was approximately 1.5 mm (0.06 in.), while the average width of the IHDZ was approximately 0.5 mm (0.02 in.).

Similar trends were evident in the other profiles of Fig. 14 B, C and D. In each case, the axial position where the slope deviated from the baseline produced by the base material may be interpreted as the outer edge of the OHDZ, while the positions of the two symmetrically disposed maxima may be considered as the approximate boundary between the inner and outer HDZ.

The width of the inner and outer HDZs increased with increasing radial distance over the range shown. Since rotation of the specimen did not involve any motion at the axial centerline, an average profile could not be obtained exactly at the center. Close to the axial centerline the entire HDZ was very narrow, and the homogenized IHDZ was not fully resolved. Farther away from the axial centerline the HDZ became wider and the weakly scattering homogenized IHDZ was more clearly discernible. The average width of the IHDZ increased from approximately 0.4 mm (0.016 in.) at a radial distance of 1.27 mm (Fig. 14A) to about 0.9 mm (0.035 in.) at a distance of

8.89 mm from the axial centerline — Fig. 14D. The average width of the OHDZ increased from about 1.7 mm (0.065 in.) to greater than 3.7 mm (0.15 in.) over the same span of radial distance. The exact width of the OHDZ at 8.89 mm from the axial centerline could not be determined from the axial backscattering data since the amplitude of the backscattered signal did not reach a baseline over the distances studied. Note that these dimensions are consistent with those of the optical micrographs in Fig. 7 and the acoustic micrograph in Fig.10A.

Radial Ultrasonic Backscattering

Radial ultrasonic backscattering measurements provided the overall widths of the HDZ at a fixed radial position (at 4 mm from the outer surface or at 8.7 mm from the axial centerline). Figure 15 shows the average radial backscattering profiles for the LAF and HAF welds. As shown in Figs. 6, 7 and 10, the bands of the base material microstructure were preferentially oriented in the axial direction as a result of the original extrusion processing. Consequently, radial ultrasonic waves were strongly scattered by the base material. In the OHDZ, the flow lines turned in the radial direction and produced much weaker scattering, while the homogenized IHDZ caused little scattering from any inspection direction. As a result, the entire HDZ appeared as a weakly scattering region surrounded by the strongly scattering base material. Because of misalignments during welding, the local thickness of the HDZ can change as much as 10% between the thinnest and thickest points separated by 180 deg. The average total width of the OHDZ at a distance of 4 mm (0.01 in.) from the periphery (*i.e.*, at a radial distance of 8.7 mm [0.35 in.] from the axial centerline) was found to be approximately 4 mm (0.16 in.) for both the LAF and HAF welds. These dimensions are consistent with corresponding dimensions obtained from Figs. 7, 10A and 14D.

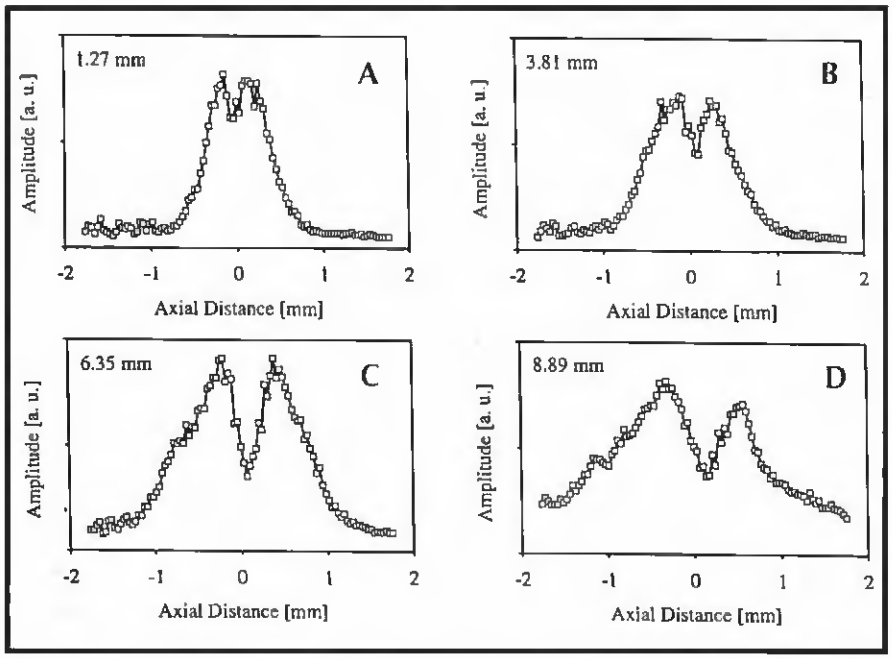

Fig. 14 — Averaged axial backscattering profiles from HAF weld at four different radial distances from the axial centerline.

Discussion

Advantages and Limitations of the UE Techniques

As mentioned previously, microstructural characterization of welds normally relies on the use of OM and SEM. In this study, the flow line patterns and weld dimensions were determined throughout the entire volume of the IFR welds using OM and SEM by repeated sectioning, grinding and polishing of the samples. However, this course of action was time consuming, and the measurement accuracy was limited by the precision of sample preparation. Attempts were made to maintain transverse metallographic specimens (such as those in Fig. 8) parallel to the weld centerline. Determination of the position of the final transverse surface with respect to some reference position was also required. Additionally, care was taken to ensure that longitudinal sections (such as those in Figs. 6 and 7) coincided as closely as possible with the prime meridian of the joined cylinders. Nonetheless, some amount of measurement error was introduced during sample preparation. These problems were further compounded by the misalignment of the two cylindrical samples that introduced slight spatial variations in weld dimensions.

The use of ultrasonic methods for the detection of weld flaws such as cracks, porosity and incomplete penetration is well established (Refs. 27, 28). This study represents one of the first efforts to utilize ultrasonic methods for microstructural characterization of welds. The problems associated with measurement errors due to sample preparation discussed above were largely avoided with the UE techniques used in this study. The penetrating nature of the ultrasonic waves largely eliminated the need for sectioning and surface preparation and allowed for nondestructive evaluation (with the exception of the acoustic microscopy technique). Computer automation of the UE procedures provided rapid identification of microstructural features throughout the weld volume, and problems with variations in weld dimensions due to misalignment were overcome by rotating the sample or gating the signal to provide an averaged response.

The ultrasonic techniques were self-consistent in that microstructures and dimensions of the weld zones found with one technique matched those ascertained using the other UE techniques. More importantly, the microstructural features and weld dimensions determined with the UE techniques closely correlated with those found using OM and SEM. Comparison of the capabilities of the UE procedures to those of OM and SEM reveals advantages and limitations inherent to each method. The advantages accrued by the UE procedures via elimination of sample preparation are offset by their lower resolution. Conversely, the greater accuracy of measurement afforded by the increased resolution of OM is limited by the problems associated with misalignment and preparation discussed above. Of course, the even greater resolution of the SEM provides still better accuracy of measurement. An exact comparison of the dimensions determined using OM and UE is not warranted owing to the use of different samples, to the different physical mechanisms associated with creating the images (optical vs. acoustic) and to the inaccuracies inherent to each method. Nonetheless, the UE methods comple-

ment OM and SEM by providing similar microstructural information over the size scales examined in this study.

Applications of the UE Methods

The C-scan images and ultrasonic micrographs provided data on the final patterns of flow lines from two orthogonal perspectives. The information obtained with the two techniques from a single sample can be computer integrated to provide a 3-D map of the final pattern of flow lines throughout the OHDZ. The flow patterns in the OHDZs of the IFR welds varied with time from the original configuration in the base material to the final conditions reflecting the integrated displacement history of the OHDZs during the weld cycle. Equations for the displacements (Ref. 37) and strain rates (Refs. 22, 38) during the forge phase of direct drive friction welding have been derived, but details of the plastic flow of material arising from IFR welding are currently not well known. Unfortunately, the tangents to the flow lines are not necessarily parallel to the vectors of the displacement field for plastic flow. Hence, the final flow line patterns shown in this paper cannot be used to accurately determine time resolved data concerning displacement, strain or strain rate. However, they can be used to corrohorate the final results of various computational process models for IFRW (Refs. 21–23, 39, 40).

Ultrasonic evaluation of "declutched" or interrupted IFR welds (Refs. 41, 42) can provide even more useful information on microstructural development in the joint area at discrete times during the welding process. In principle, plastic strains can he determined as functions of position in the OHDZ from the 3-D maps of a series of interrupted welds and compared for welds made with different parameters. The time resolved strain data may also prove useful in confirming the results of computational models for IFRW. In addition, the temporal development of the IHDZ can be studied with interrupted welds.

As discussed previously, the techniques employed in this study exploited the differences in ultrasonic scattering due to variations in the spatial distribution and alignment of the reinforcement. With minor modifications, the UE procedures described here may be used to study IFR welds on other materials containing two (or more) banded phases that differ in stiffness and/or density. Examples of such materials include other banded MMCs, low-carbon steels that exhibit ferrite/pearlite banding, and free machining steels with sulfide stringers aligned parallel to the rolling direction.

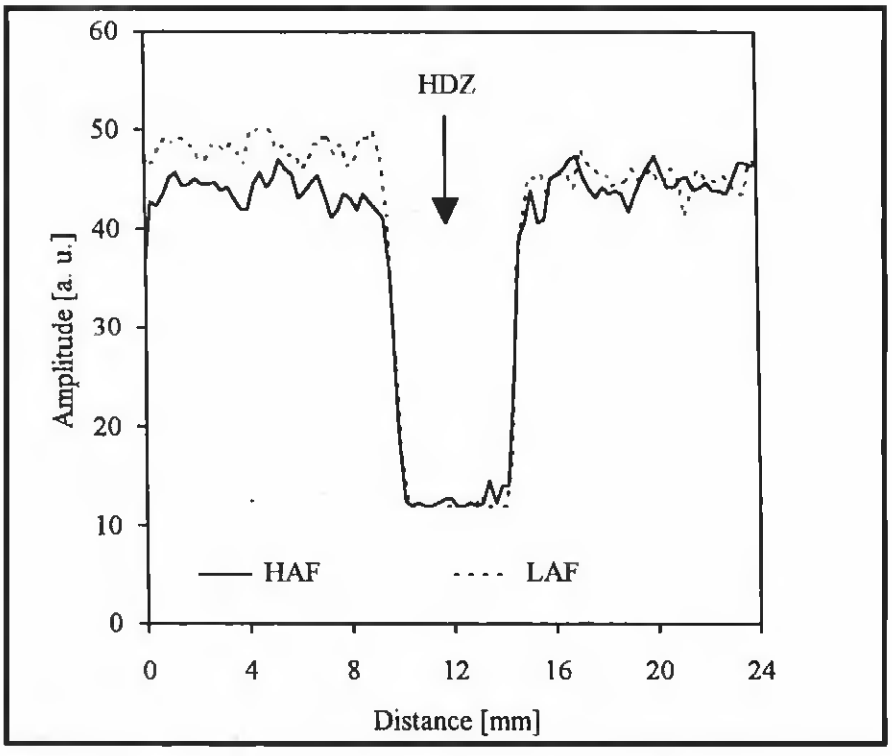

Fig. 15 — Averaged radial backscattering profiles for HAF and LAF welds.

In addition, the presence of martensite in welds in steels can be discerned due to its high stiffness relative to ferrite.

Continuous banding may not be required to produce appreciable variations in ultrasonic scattering in IFR welds of some materials. The UE techniques may also be adapted to materials with discrete "aligned" second phases such as borated stainless steels as well as whisker and short fiber reinforced MMCs that are extruded to align the long dimension of the reinforcement with the extrusion direction.

Finally, the UE procedures may also be adapted to other processes involving MMCs and similar materials. For instance, they can be utilized to examine fusion welds of MMCs, oxide dispersion strengthened (ODS) materials and hardfacing alloys where agglomeration and/or segregation of the reinforcement have been reported. Similarly, these methods might be used to characterize reinforcement redistribution in castings of MMCs and to investigate reinforcement loading along the bondline during brazing and diffusion bonding of MMCs.

Flow Line Distributions

Information concerning the final arrangement of flow lines in the OHDZ of the IFR welds gathered from previous figures can be summarized in a schematic drawing of a cylinder of radius R. Figure 16 is an exploded view schematic that depicts the paths of flow lines originating from three different radial locations in the cylinder: R_1, R_2 and R_3 (where $R>R_1>R_2>R_3$). The cylinder shown in Fig. 16 is one of the two used to produce the weld. The IHDZ and the second cylinder are omitted in this figure for clarity. Axial, radial and tangential directions are defined by the axes shown in the figure.

The three shaded surfaces represent horn-shaped vortices of different sizes that increase in radius from R_i to R_i' (where i = 1, 2 or 3) with decreasing distance from the weld centerline. The flow lines follow paths along the surfaces of the vortices as indicated by the spiraling arrows. Note that the dimensions of the arrows are not meant to indicate the magnitude. Moreover, recall that the arrows represent the paths of the final flow lines and are not necessarily parallel to the displacement or strain vectors of plastic flow. For greater ease of illustration, the three vortices are separated in this exploded view. In reality, the vortices fit together concentrically as shown in the inset. The boundary between the OHDZ and IHDZ is indicated by the surface marked A in the inset.

Consider the path of the flow lines originally located at R_1. Far from the weld centerline, the flow lines from the original extrusion processing are parallel to the axial centerline as indicated by the straight arrow. At the outer edge of the

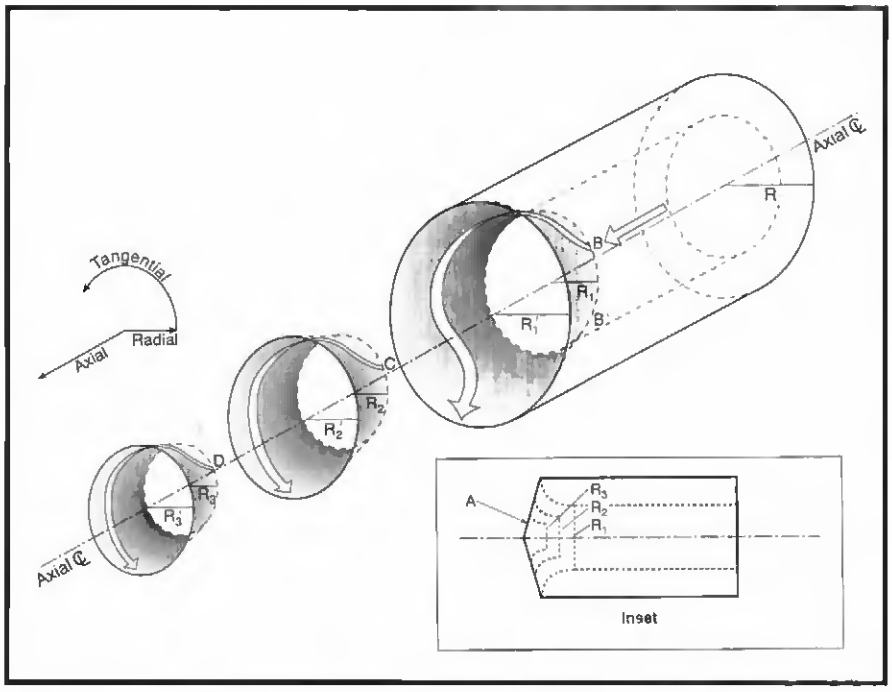

Fig. 16 — Exploded view schematic of flow lines in the OHDZ of an IFR weld. Arrows show paths for flow lines originating at three different radial positions. For a given starting radial position, the flow lines follow spiraling paths on the surface of the different shaded vortices. Inset shows side view (not exploded). See text for further details.

OHDZ (position B), the flow lines turn gradually and follow spiraling paths with continually increasing radius on the surface of the shaded vortex. Near the IHDZ/OHDZ boundary at R_1' on surface A, the paths of the flow lines lie entirely in a plane parallel to the weld centerline, and for the HAF weld, the path is almost entirely in the radial direction. Flow lines originating at B', also located at R_1 but tangentially displaced from B, follow similar paths that parallel those from B.

Flow lines originating at R_2 (position C) follow slightly different spiral paths on a second vortex of smaller radius. The flow line paths proceeding from R_2 (on the second vortex) have a weaker radial component relative to those at greater radial distances (on the first vortex) as suggested by the C-scan images in Figs. 11–13. Similarly, the paths of the flow lines originating at R_3 (position D) have an even smaller radial component than those originating at R_2 (position C).

Process/Structure/Property Relations

As discussed in the Introduction section of this paper, the fracture resistance of forgings and IFR welds depends on the orientation of the flow lines with respect to the applied stress field. Microstructural analysis has shown that extrusion of the base material during primary production resulted in the development of flow lines in the form of alternating SiC-rich and SiC-depleted bands oriented parallel to the extrusion direction. Moreover, plastic flow in the OHDZ during welding has been shown to produce realignment or reorientation of the bands. Knowledge of the patterns of flow lines in IFR welds can be useful in designing and producing welds with minimal loss in toughness. This knowledge is even more important for IFR welds in 8009/SiC/11p since MMCs typically exhibit lower strains to failure and fracture toughness relative to their monolithic counterparts (Refs. 43, 44).

The fracture resistance of IFR welds in 8009/SiC/11p is determined by several microstructural features including the grain size and the orientation of the flow lines (the SiC-rich and SiC-depleted bands) as well as the volume fraction, size and distribution of the intermetallic dispersoids and the SiC reinforcement. Despite cracking of some of the larger SiC particles, little change in the SiC size distribution (relative to the base material) was observed in the HDZs of either the HAF or LAF welds produced in this investigation. Additionally, IFRW produced a homogenous IHDZ with a uniform distribution of SiC. Previous studies on the same welds using transmission electron microscopy (TEM) revealed no significant differences in the grain size or the volume fraction, size and distribution of the dispersoids between the base material and the weld regions (Ref. 45). Hence, the major microstructural change involved the redistribution of SiC in the IHDZ and reorientation of the flow lines in the OHDZ. Consequently, lower strains to failure (relative to the base material) in subscale tensile samples machined from these IFR welds (Refs. 33, 45) may be attributed mainly to the realignment of the bands since all of the weld tensile samples failed in the OHDZ through regions where the flow lines were aligned with the maximum resolved shear stress at 45 deg to the tensile axis.

Lower measured values of elastic modulus (Ref. 45) for the same weld tensile samples (with respect to the base material) may also be ascribed to the realignment of the bands. For the sake of discussion, the material may be considered as a composite of alternating stiff SiC-rich bands and compliant SiC-depleted bands. In the base material tensile samples, the tensile axis was parallel to the extrusion direction and the alternate SiC-rich/SiC-lean bands were loaded in an isostrain condition (Ref. 46), resulting in a high composite modulus. In contrast, the bands in the OHDZs of the weld tensile samples reoriented perpendicular to the tensile axis were loaded in a condition similar to an isostress condition (Ref. 46). Hence, the higher stiffness of the SiC-rich bands was not exploited in this orientation, and lower values of elastic modulus were found for the weld tensile samples. The patterns of microstructural banding may also affect the creep and fatigue properties of the welds.

Process Implications

The information provided by the UE methods in this study also contributes to an improved understanding of plastic flow resulting from the IFRW process. While the final flow line patterns cannot be used to determine quantitative information concerning the displacement or flow fields for material during welding, they can be used to make qualitative inferences with respect to the directions of displacement late in the weld cycle. The findings of this study confirm that the material in the OHDZs of IFR welds was displaced in the axial, radial and tangential directions during welding. Moreover, the strength or dominance of the components of flow evidently varied with axial and radial position for a constant weld axial force. For example, the axial components of displacement seemed to diminish with decreasing distance from the weld centerline for both the LAF and HAF welds. Hence, plastic flow near the inner edge of the OHDZ appeared to be largely restricted to planes parallel to the weld centerline.

The differences in the flow line patterns in the OHDZs of the HAF and LAF

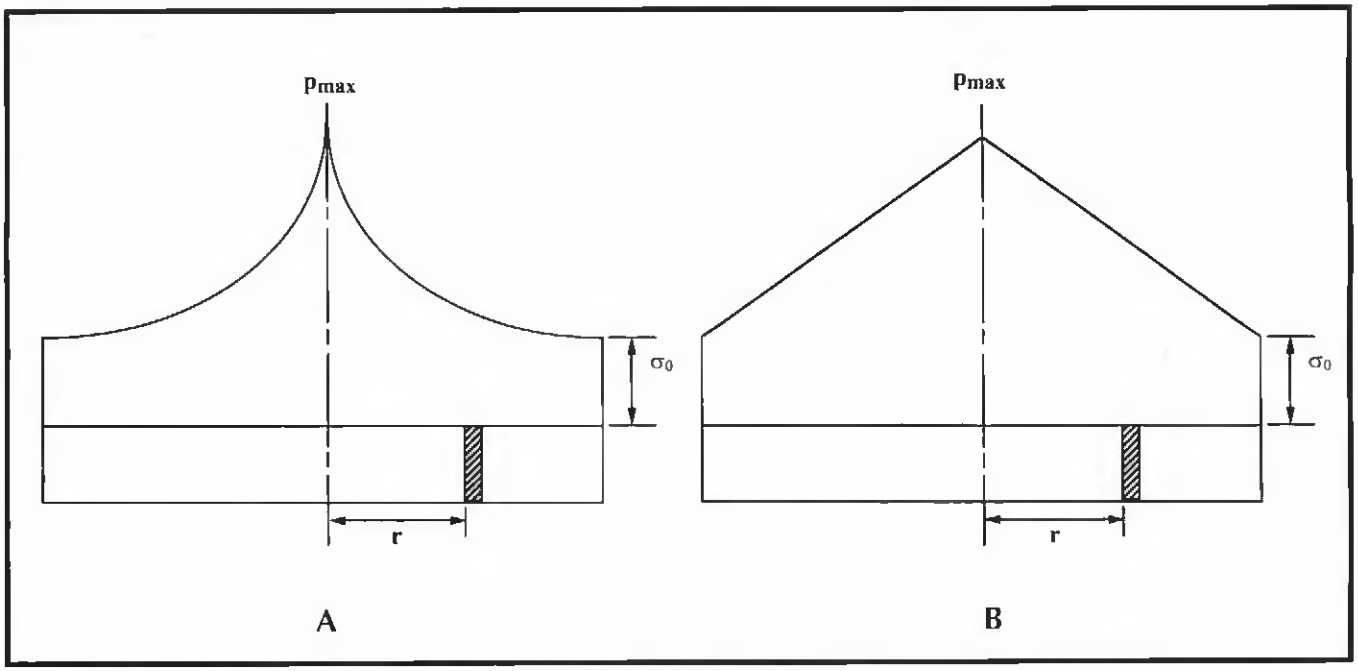

Fig. 17 — Schematic representations of friction hills for (A) sliding friction and (B) sticking friction (adapted from Ref. 49). The axial pressure falls from a maximum at the axial centerline to the yield stress (σ_0) at the periphery.

welds suggest that the strength of the different flow components also varied with the axial force used for welding (*i.e.*, the flow fields varied with axial force). Specifically, the radial components of displacement in the OHDZ of the HAF welds appeared larger than those at the same positions in the LAF welds. In fact, plastic flow near the periphery of the HAF welds seemed to occur almost entirely in the radial direction. This observation suggests that the material at shorter radial distances from the axial centerline was constrained from moving radially by the surrounding material. Conversely, material near the periphery was less constrained and was evidently freer to move in the radial direction.

One possible explanation for the alterations in flow direction with radial distance for the HAF welds involves a variation in normal pressure (*i.e.*, axial stress) during welding. While several researchers assume the normal pressure to be uniform across the faying surfaces for calculations of temperature (Refs. 14, 22, 47), the pressure during IFRW likely varies with radial distance in a manner similar to that found for axisymmetric compressive forging of a flat circular disk under plane strain conditions (Refs. 48–50).

The normal pressure across a flat disk under plane strain conditions in compression can be shown to decrease from a maximum at the centerline to a value equal to the yield stress at the periphery (Refs. 48, 49). Depending on the boundary conditions used in the derivation, the pressure across the interface can vary either linearly (assuming conditions of sticking friction) or exponentially (assuming conditions of sliding or lubricated friction) with radial distance. While the equations that result from these derivations represent idealized extremes in behavior, they have been shown to adequately describe the situation as similar trends have been found through experimentation (Ref. 50). A plot of normal pressure against radial distance for this application is often termed the friction hill. Schematic friction hills for sticking and sliding friction conditions are shown in Fig. 17 (Refs. 48, 49).

While the conditions found during IFRW are not identical to those for forging of a flat disk (there is no rotational motion in forging for example), it is not unreasonable to suggest that the radial pressure variations are similar in nature. The interfacial friction conditions and hence the variations in axial pressure conditions presumably change with time for IFRW. Very early in the weld cycle, sliding friction occurs at the interface before any bonding takes place. Shortly thereafter, seizure takes place at points along the interface, and conditions of sticking friction prevail. Bonding ensues during this period and the IHDZ begins to develop and spread across the entire interface (Ref. 42). Finally, a condition of lubricated sliding friction may ensue as the fully developed IHDZ acts as a viscoplastic layer of lubricant between the opposing sides of the relatively stiff OHDZ. Regardless of the friction conditions, the lower normal pressures near the periphery appear to provide less lateral constraint on the material in the OHDZ and allows greater ease of radial flow, which gives rise to the flow patterns observed in the HAF welds.

A second rationalization for the variations in flow patterns with radial distance for the HAF welds allows for the possibility of continued deformation of the material of the OHDZ at the end of the weld cycle. The higher axial force may be sufficient to produce further deformation of the material in the OHDZ (that remains heated) after the rotating part stops, similar to that which occurs in the forging phase of direct-drive friction welding. As a consequence, predominantly radial plastic flow is expected to occur, as in direct-drive friction welding, since no rotational component of motion remains. Regardless of the cause of the variations of flow patterns, further work aimed at discerning the evolution of flow with time during IFRW is required, and the UE procedures may prove useful in this regard.

Conclusions

1) This study represents one of the first efforts to utilize ultrasonic methods for microstructural characterization of welds. The SiC particles in the as-received extrusion were distributed into alternate SiC-rich and SiC-depleted bands oriented parallel to the extrusion direction. IFR welding resulted in a homogeneous distribution of SiC particles in the IHDZ and realignment of the alternate SiC-rich and SiC-depleted bands in the

OHDZ. The ultrasonic procedures described in this study exploited the variations in ultrasonic scattering provided by changes in the spatial distribution of the SiC particles.

2) The ultrasonic techniques allowed rapid determination of the patterns of plastic flow lines in IFR welds on 8009/SiC/11p, as well as the dimensions of the inner and outer HDZs as functions of position. The information on the final patterns of flow lines and weld dimensions can be used to corroborate the final results of computational process models for IFRW. The ultrasonic methods described in this study may also be employed to study IFR welds on similar banded or aligned materials and can likely be adapted to other processes involving MMCs and comparable materials.

3) The ultrasonic techniques were self-consistent in that weld microstructures and dimensions determined with one procedure matched those found with the other UE techniques. More importantly, the microstructural features and sizes of the weld zones determined with the UE methods closely correlated with those observed using OM and SEM. The UE methods complement OM and SEM by providing similar microstructural information over the size scales examined in this study.

4) Results of this study also contribute to a greater understanding of process/structure/property relations in IFR welds on 8009/SiC/11p. The flow lines of SiC-rich and SiC-depleted bands followed spiral-shaped paths in the OHDZ of the IFR welds. Lower values for strain to failure and elastic modulus (relative to the base material) in subscale tensile samples from these welds tested in previous studies were attributed to realignment of the SiC-rich and SiC-depleted bands in the OHDZ.

5) Results confirm that the material in the OHDZ of the IFR welds was displaced in the axial, radial and tangential directions. The strength or dominance of the components of displacement or flow varied with axial and radial positions for a constant weld axial force. The components of flow also varied with the axial force used for welding.

Acknowledgments

The authors wish to thank AlliedSignal, Inc., of Morristown, N.J., for supplying the material used in this study. The authors also wish to acknowledge Dave Brewer of Ohio State University (OSU) for assistance in machining of samples, Tim Stotler of Edison Welding Institute for help in producing the IFR welds, Bill Hartlieb of OSU for assistance with Fig. 16, as well as Dr. R. J. Grylls and Dr. J. M Wiezorek of OSU for their careful review of this manuscript. The authors additionally thank the Army Research Office under contract number DAAL03-92-G-0148 for partial funding of this project. Finally, Mr. Lienert would like to express his appreciation to the American Welding Society for its continued support through an AWS Foundation Fellowship.

References

1. Zedalis, M. S., Bryant, J. D., Gilman, P. S., and Das, S. K. 1991. High-temperature discontinuously reinforced aluminum. *JOM* 43(8): 29–31.

2. Skinner, D. J. 1988. The physical metallurgy of dispersion strengthened Al-Fe-V-Si alloys. *Dispersion Strengthened Aluminum Alloys*, eds. Y. W. Kim and W. M. Griffith, pp. 181–197, Warrendale, Pa., The Minerals, Metals & Materials Society.

3. Raybould, D. 1988. Forming of rapidly solidified elevated temperature aluminum alloys produced by planar flow casting. *Dispersion Strengthened Aluminum Alloys*, eds. Y. W. Kim and W. M. Griffith, pp. 199–215, Warrendale, Pa., The Minerals, Metals & Materials Society.

4. Bye, R. L., Kim, N. J., Skinner, D. J., Raybould, D., and Brown, A. M. 1986. Rapidly solidified powder metallurgy aluminum alloys prepared from melt spun ribbons. *Proceedings of Processing of Structural Metals by Rapid Solidification*, eds. F. H. Froes and S. J. Savage, pp. 283–289, Materials Park, Ohio, ASM International.

5. McKimpson, M. G., Pohlenz, E. L., and Thompson, S. R. 1993. Evaluating the mechanical properties of commercial DRA. *JOM* 45(1): 26–29.

6. Zedalis, M. S., and Skinner, D. J. 1989. Young's moduli of Al-Fe-X-Si alloys and Al-Fe-V-Si base metal matrix composites. *Light-Weight Alloys for Aerospace Applications*, eds. E. W. Lee *et. al.*, pp. 335–344, Warrendale, Pa., The Minerals, Metals & Materials Society.

7. Zedalis, M. S., Peltier, J. M., and Gilman, P. S. 1989. High temperature Al-Fe-V-Si base matrix composites: mechanical properties and microstructure. *Light-Weight Alloys for Aerospace Applications*, eds. E. W. Lee *et. al.*, pp. 323–334, Warrendale, Pa., The Minerals, Metals & Materials Society.

8. Sampath, K., and Baeslack III, W. A. 1993. Selection and weldability of dispersion-strengthened aluminum alloys. *ASM Handbook Vol. 6 — Welding, Brazing and Soldering*. p. 541, Materials Park, Ohio, ASM International.

9. Lienert, T. J., Lane, C. T., and Gould, J. E. 1993. Selection and weldability of aluminum metal-matrix composites. *ASM Handbook Vol. 6 — Welding, Brazing and Soldering*, p. 554, Materials Park, Ohio, ASM International.

10. Duffin, F. D., Dickson G. R., and Bahrani, A. S. 1972. Research friction-welding with hydrostatic drive. *Metal Construction and British Welding Journal* 4(5): 161–166.

11. Elmer, J. W., and Kautz, D. D. 1993. Fundamentals of friction welding. *ASM Handbook Vol. 6 — Welding, Brazing and Soldering*. p. 150, Materials Park, Ohio, ASM International.

12. Dieter, G.E., 1986. *Mechanical Metallurgy*, p 303, New York, N.Y., McGraw-Hill.

13. R. L. O'Brien, ed. 1991. *Welding Handbook Vol. 2*, 8th ed., p. 740, Miami, Fla., American Welding Society.

14. Wang, K. K., and Nagappan, P. 1970. Transient temperature distribution in inertia welding of steels. *Welding Journal* 49(9): 419-s to 426-s.

15. Baeslack III, W. A., and Hagey, K. S. 1988. Inertia friction welding of rapidly solidified powder metallurgy aluminum. *Welding Journal* 67: 139-s to 149-s.

16. Hou, K. H., and Baeslack III , W. A. 1990. Electron microscopy of inertia-friction weldments in a rapidly solidified Al-Fe-Mo-V alloy. *Journal of Materials Science* 25: 2642–2653.

17. Koo, H. H., Krishnaswamy, S., and Baeslack III, W. A. 1991. Characterization of inertia-friction welds in a high-temperature RS/PM Al-8.5Fe-1.3V-1.7Si Alloy (AA-8009). *Materials Characterization* 26: 123–136.

18. Koo, H. H., and Baeslack III, W. A. 1992. Friction welding of a rapidly solidified Al-Fe-V-Si alloy. *Welding Journal* 71(5): 147-s to 169-s.

19. Cola, M. J. 1992. *Inertia-friction welding of particulate-reinforced aluminum matrix composites*, M.S. dissertation, Columbus, Ohio, The Ohio State University.

20. Cola, M. J., and Albright, C. E. 1992. Inertia-friction welding of particulate-reinforced aluminum composites — initial studies. *Proceedings of the 3rd International Conference on Trends in Welding Research*. eds, S. A. David and J. M. Vitek, pp. 1139-1146, Materials Park, Ohio, ASM International.

21. Midling, O. T., and Grong, O. 1992. Continuous drive friction welding of SiC particulate reinforced aluminium composites. *Proceedings of the 3rd International Conference on Trends in Welding Research*, eds. S. A. David and J. M. Vitek, pp.1147–1151, Materials Park, Ohio, ASM International.

22. Midling, O. T., and Grong, O. 1994. A process model for friction welding of Al-Mg-Si alloys and Al-SiC metal matrix composites I. HAZ temperature and strain rate distribution. *Acta Metallurgica et Materialia* 42(5): 1595–1609.

23. Midling, O. T., and Grong, O. 1994. A process model for friction welding of Al-Mg-Si alloys and Al-SiC metal matrix composites II. HAZ microstructure and strength evolution. *Acta Metallurgica et Materialia* 42(5): 1611–1622.

24. Shoemaker, L. E. 1986. Joining techniques for a ferritic oxide dispersion strengthened alloy. *Proceedings of the International Conference on Trends in Welding Research*, ed. S. A. David, pp. 371–377, Materials Park, Ohio, ASM International.

25. Ambroziak, A., and Lison, R. 1993. Welding and brazing ODS materials. *Welding Research Abroad* 12: 10–15.

26. Hertzberg, R. W. 1989. *Deformation and Fracture Mechanics of Engineering Materials*, p. 357, New York, N.Y., Wiley.

27. ASM Committe on Ultrasonic Inspection. 1976. Ultrasonic inspection. *ASM Metals Handbook Vol. 11*, 8th ed., eds. H. E. Boyer and W. J. Carnes, pp. 161–198, Materials Park, Ohio, ASM International.

28. Bray, D. E., and Stanley, R. K. 1989. *Nondestructive Evaluation*, p. 47, New York, N.Y., McGraw-Hill.

29. Nagy, P. B., and Adler, L. 1992. Ultra-

sonic evaluation of solid-state bonds. *Materials Evaluation* 12: 1328–1337.

30. Nagy, P. B., and Adler, L. 1988. Ultrasonic NDE of solid-state bonds: Inertia and friction welding. *Journal of Nondestructive Evaluation* 7(3): 199–215.

31. Nagy, P. B., Lienert, T. J., Adler, L., and Baeslack III, W. A. 1995. Novel nondestructive evaluation techniques for inertia-friction welds in a SiC-reinforced high-temperature aluminum alloy. *Review of Progress in Quantitative Nondestructive Evaluation, Vol. 14*, eds. D. O. Thompson and D. E. Chimenti, pp. 1545–1552, Plenum Press.

32. Briggs, A. 1992. *Acoustic Microscopy*. New York, N.Y., Oxford Press.

33. Lienert, T. J., Baeslack III, W. A., Ringnalda, J., and Fraser, H. L. 1996. Inertia-friction welding of SiC-reinforced 8009 aluminum. *Journal of Materials Science* 31: 2149–2157.

34. Yang, J., Cady, C., Hu, M. S., Zok, F., Mehrabian, R., and Evans, A. G. 1990. Effects of damage on the flow strength and ductility of a ductile Al alloy reinforced with SiC particulates. *Acta Metallurgica et Materialia* 38(12): 2613–2619.

35. Bao, G. 1992. Damage due to fracture of brittle reinforcements in a ductile matrix. *Acta Metallurgica et Materialia* 40(10): 2547–2555.

36. Brechet, Y., Newell, J., Tao, S., and Embury, J. D. 1993. A note on particle comminution at large plastic strains in Al-SiC composites. *Scripta Metallurgica et Materialia* 28: 47–51.

37. Rich, T., and Roberts, R. 1971. The forge phase of friction welding. *Welding Journal* 51(3): 137-s to 145-s.

38. Rakhimov, A. E., Li, Z., and North, T. H. 1996. Theoretical modeling of MMC base material friction joining. *Canadian Metallurgical Quarterly* 35(3): 285–289.

39. Nied, H. A. 1992. Finite element simulation of inertia welding. *Abstracts of the 73rd AWS Annual Meeting*, pp. 187–188, Miami, Fla., American Welding Society.

40. Soucail, M., Moal, A., Nazé, L., Massoni, E., Levaillant, C., and Bienvenu, Y. 1992. Microstructural study and numerical simulation of inertia friction welding of Astroloy. *Superalloys 1992*, eds. S. A. Antolovich *et. al.*, pp. 847–856, Warrendale, Pa., The Minerals, Metals & Materials Society.

41. Johnson, P. C., Stein, B. A., and Davis, R. S. 1966. *Report on inertia welding to the Caterpillar Tractor Company*, Cambridge, Mass., Arthur D. Little, Inc.

42. Rao, M., and Hazlett, T. H. 1970. A study of the mechanisms involved in friction welding of aluminum alloys. *Welding Journal* 50(4): 181-s to 188-s.

43. Mortensen, A. 1990. A review of the fracture toughness of particle reinforced aluminum alloys. *Fabrication of Particulate Reinforced Metal Matrix Composites*, eds. J. Masounave and F. G. Hamel, pp. 217–233, Materials Park, Ohio, ASM International.

44. Hunt, W. H., Osman, T. M., and Lewandowski, J. J. 1993. Micro- and microstructural factors in DRA fracture resistance. *JOM* 45(1): 30–35.

45. Lienert, T. J. 1995. Characterization of inertia-friction welds in SiC-reinforced 8009 aluminum. M.S. thesis, Columbus, Ohio., The Ohio State University.

46. Courtney, T. H. 1990. *Mechanical Behavior of Materials*, p. 223, New York, N.Y., McGraw-Hill.

47. Vill, V. I. 1962. *Friction Welding of Metals*, pp. 23–28, New York, N.Y., Reinhold Publishing.

48. Hosford, W. F., and Caddell, R. M. 1983. *Metal Forming: Mechanics and Metallurgy*, pp. 120–128, Englewood Hills, N.J., Prentice-Hall.

49. Dieter, G. E. 1986. *Mechanical Metallurgy*, pp. 539–549, New York, N.Y., McGraw-Hill.

50. van Rooyen, G. T., and Backofen, W. A. 1960. A study of interface friction in plastic compression. *International Journal of Mechanical Science* 1(1): 1–27.